

Atlas is Your Perfect Context: One-Shot Customization for Generalizable Foundational Medical Image Segmentation

Ziyu Zhang^{1*}, Yi Yu^{2*}, Simeng Zhu², Ahmed Aly², Yunhe Gao³, Ning Gu¹, Yuan Xue^{2†}

¹Nanjing University ²The Ohio State University ³Stanford University

Abstract

Accurate medical image segmentation is essential for clinical diagnosis and treatment planning. While recent interactive foundation models (e.g., nnInteractive) enhance generalization through large-scale multimodal pretraining, they still depend on precise prompts and often perform below expectations in contexts that are underrepresented in their training data. We present *AtlasSegFM*, an atlas-guided framework that customizes available foundation models to clinical contexts with a single annotated example. The core innovations are: 1) a pipeline that provides context-aware prompts for foundation models via registration between a context atlas and query images, and 2) a test-time adapter to fuse predictions from both atlas registration and the foundation model. Extensive experiments across public and in-house datasets spanning multiple modalities and organs demonstrate that *AtlasSegFM* consistently improves segmentation, particularly for small, delicate structures. *AtlasSegFM* provides a lightweight, deployable solution one-shot customization of foundation models in real-world clinical workflows. The code will be made publicly available.

1. Introduction

Interactive segmentation has emerged as a promising approach in medical imaging, enabling precise and customizable delineation by incorporating user input [15, 21, 22, 30]. Unlike end-to-end methods, which may struggle to generalize across diverse anatomical structures and imaging modalities, interactive segmentation allows clinicians to guide the model so that results align with clinical expectations [13, 40]. In clinical practice, segmentation demands vary widely such as abdominal organ delineation, vascular segmentation in angiography, and organs-at-risk identification in radiotherapy, each with distinct anatomical complexity, task-specific requirements, and imaging protocols. Moreover, physicians may differ in how they define and prioritize structures, par-

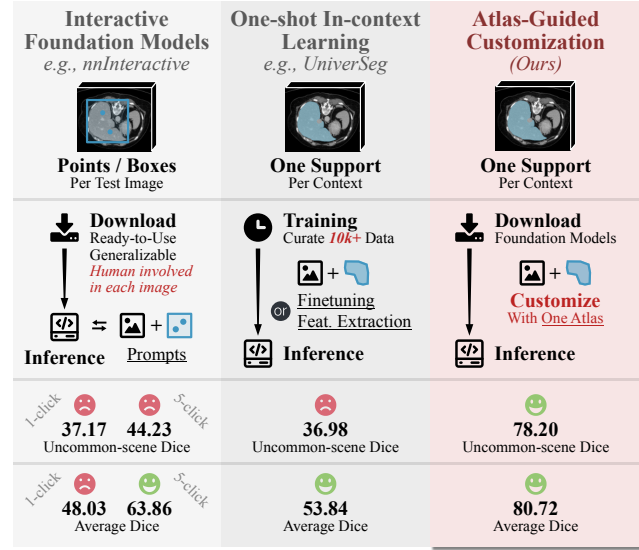


Figure 1. Comparison of three segmentation paradigms. Our method adapts off-the-shelf segmentation foundation models to each target context using one atlas. “Uncommon-scene Dice” averages BrainRT (organs-at-risk) and Fe-MRA (vessels).

ticularly for small yet clinically critical regions, making it essential for segmentation tools to accommodate individual judgment. The ability to perform segmentation on demand, customized to specific clinical contexts or physician instructions, is therefore crucial for rare conditions, patient-specific variations, or limited annotated data, underscoring the need for flexible, adaptive, and clinically intuitive solutions in medical image analysis.

Existing customized segmentation typically relies on two main approaches: interactive segmentation and In-Context Learning (ICL). Interactive segmentation leverages user inputs, such as scribbles or clicks, to iteratively refine predictions and adapt to specific cases. While methods like nnInteractive [13] and ScribblePrompt [39] demonstrate its potential, they often require multiple interactions and rely heavily on the quality of user inputs. In contrast, ICL enables segmentation by providing contextual examples or prompts during inference, without the need for interaction or

*These authors contributed equally to this work.

†Corresponding author. Email: xue.643@osu.edu

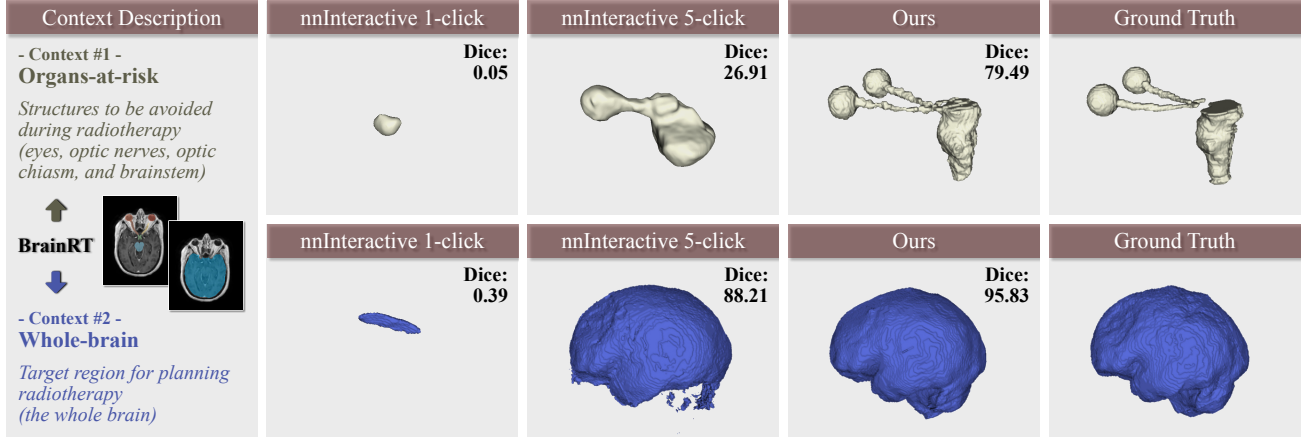


Figure 2. Visual comparisons with recent interactive method (i.e., nnInteractive [13]) on the BrainRT dataset for radiotherapy. nnInteractive performs far below expectation in context #1 (organs-at-risk), an uncommon contexts underrepresented in its training data.

user input. ICL methods such as UniverSeg [3] and Iris [6] have shown the ability to generalize across various tasks and datasets by leveraging in-context examples, using reference examples or prompts to segment for specific scenarios.

As shown in Fig. 1, interactive methods offer flexibility by leveraging user inputs (e.g., points or boxes) to iteratively refine predictions during inference, whereas one-shot in-context learning methods use a single support example per context and require no interaction at inference. However, current ICL methods require large, carefully annotated datasets and training or extensive fine-tuning, making them both resource-intensive and time-consuming [3, 6, 29, 37]. Meanwhile, the growing availability of segmentation foundation models suggests an alternative strategy: instead of training a new model for each task, we can customize strong pretrained models to each clinical context.

Moreover, interactive foundation models still struggle when prompts are ambiguous or when the target structure is rare or small [13, 21]. As shown in Fig. 2, interactive methods perform well in common scenarios, such as whole brain segmentation, achieving a Dice score of 88.21% with 5-click interaction. However, their effectiveness drops significantly in delicate structures, with the Dice score falling to 26.91% for organs-at-risk, where the targets are small, delicate structures embedded in complex context. This gap reflects both the limitations of pre-training data coverage and the absence of explicit contextual information in spatial prompts, which impedes generalization to unseen categories and fine-grained anatomy.

To address the above challenges, we propose a novel pipeline that combines structural priors of classical atlas-based segmentation with the representational power of modern segmentation foundation models. Our method leverages atlas-based registration to avoid the training burden typically associated with ICL while preserving critical structural pri-

ors in a single support example. The atlas mask serves as a context-aware prompt for interactive or non-interactive foundation models, providing more meaningful guidance and improving segmentation performance. This design enables efficient, contextually rich, and robust segmentation across diverse clinical scenarios. The main contributions of this work are as follows:

- We formalize a practically relevant task setting for medical image segmentation: one-shot customization of segmentation foundation models, where a single annotated atlas adapts any foundation model to a new clinical context.
- We present AtlasSegFM, a simple yet effective pipeline that couples globally consistent atlas registration with the local refinement ability of foundation models. A lightweight adaptive fusion module combines their complementary strengths at test time.
- We extensively evaluate AtlasSegFM on multiple public and in-house datasets across abdominal, brain, and vascular segmentation tasks. It achieves state-of-the-art accuracy and consistently surpasses existing methods, especially in underrepresented scenarios, demonstrating strong out-of-distribution robustness.

2. Related Work

2.1. Medical Image Segmentation

Medical image segmentation has long been a prominent research focus, with deep learning emerging as the dominant approach. Early deep learning methods relied on supervised learning, leading to the development of numerous state-of-the-art architectures, including U-Net variants [31, 48], Transformer-based models [5, 35, 47], and frameworks based on Mamba [18, 32, 43]. These methods have demonstrated remarkable performance across a wide range of segmentation tasks, particularly when sufficient annotated

data is available. By incorporating a fully automated pipeline design, nnU-Net [12] optimizes preprocessing, architecture, and hyperparameters for each dataset, providing a robust and adaptable solution. Its comprehensive design has set a standard for supervised learning methods in the field.

However, these methods face significant challenges when dealing with out-of-distribution data or new segmentation tasks [45]. Their performance deteriorates in scenarios that deviate from the training domain, and adapting to new or specific tasks often requires retraining the model from scratch. This process is heavily reliant on annotated data and substantial computational resources, making it impractical for deployment in highly customized clinical tasks.

2.2. Foundation Models

Foundation models have shown remarkable success in medical image segmentation [15, 30]. Some are task-specific, such as vesselFM [38], a general-purpose zero-shot 3D vascular segmentation model with strong generalization capability. To enable user-customized segmentation, another line of research has explored interactive approaches, such as MedSAM [21, 22] and nnInteractive [13]. By incorporating user prompts (e.g., clicks and bounding boxes), these methods simplify the annotation and achieve strong performance with minimal user interaction [7, 36, 39].

While these models leverage powerful pretraining on large datasets to generalize across tasks, they still face two challenges: **1)** Prompts are often ambiguous, and the models infer user intent based on prior training data. Consequently, in uncommon contexts (e.g., organs-at-risk in Fig. 2), their performance falls short of expectations. **2)** They require repeated user interactions for each image, making them inefficient for large-scale segmentation tasks or routine clinical workflows, where many patients follow similar procedures. In-context learning is a possible solution to these challenges.

2.3. In-context Learning Methods

In-context learning allows models to generalize to unseen tasks by leveraging a context set of labeled image-segmentation pairs at inference time [10, 40–42, 46]. Few-shot segmentation methods [3, 20], primarily designed to reduce labeling effort, were explored first. However, most of these methods rely on small models and limited data, and some [4, 17, 27, 33] are further fine-tuned on the target domain (referred to as cross-domain ICL). As a result, they lack the generality needed to perform arbitrary segmentation like foundation models. Therefore, some ICL studies train on larger datasets, including UniverSeg [3] and Iris [6].

With the growing availability of pretrained foundation models (see Sec. 2.2), a key limitation of these ICL approaches has become evident—they must be trained from scratch or fine-tuned on specific datasets, preventing them from leveraging the continuously improving foundation mod-

els. To address this, some studies have incorporated foundation models into ICL [44]. Their application to the medical domain is still at an early stage [19, 23, 49], with either unavailable code or limited performance. Moreover, existing ICL methods are primarily designed and evaluated on 2D images, limiting their applicability to 3D segmentation. How to fully leverage the capabilities of foundation models in ICL remains largely unexplored in the literature.

2.4. Atlas-based Segmentation

Atlas-based methods represent a classical approach to segmentation that does not require annotations or learning [11]. These methods treat segmentation as a registration problem, where the atlas is aligned to unlabeled data using optimization algorithms. Through this alignment, the structural information from the atlas can be transferred to the target image, enabling segmentation without direct supervision. Historically, atlas-based approaches iteratively minimize a cost function measuring the similarity between atlas and query [34]. More recently, some deep-learning-based registration methods have been proposed [1, 8]. By leveraging neural networks, these approaches efficiently learn the mappings from atlas to query, significantly reducing computational overhead while improving accuracy.

3. Methods

3.1. Preliminary

Medical image segmentation aims to assign a label to each pixel (or voxel) of an input image X based on its underlying anatomical structure. Formally, given an input image $X \in \mathbb{R}^{H \times W \times D}$ (e.g., CT or MRI 3D scans) and a segmentation model f_θ , the goal is to predict a label map $Y \in \mathbb{R}^{H \times W \times D}$, where each voxel $y_i \in Y$ corresponds to a predefined anatomical or pathological category. This can be formulated as $Y = f_\theta(X)$ where θ represents the parameters of the segmentation model, typically learned through supervised training on a labeled dataset $\mathcal{D} = \{(X_i, Y_i)\}_{i=1}^N$.

In clinical practice, segmentation often needs to be *Customized* for specific tasks, such as segmenting rare uncommon structures or adapting to new imaging modalities. Inspired by ICL, where a support set is used to provide domain-specific guidance, a customized segmentation task can be reformulated as:

$$Y_{query} = f(X_{query}, \mathcal{C}) \quad (1)$$

where $\mathcal{C} = (X_{support}, Y_{support})$ is the support set providing domain-specific guidance and X_{query} is the query image.

3.2. Approach Overview

Existing ICL methods rely on feature similarity between $X_{support}$ and X_{query} , which either requires extensive training and large-scale labeled data (e.g. UniverSeg[3], Iris[6])

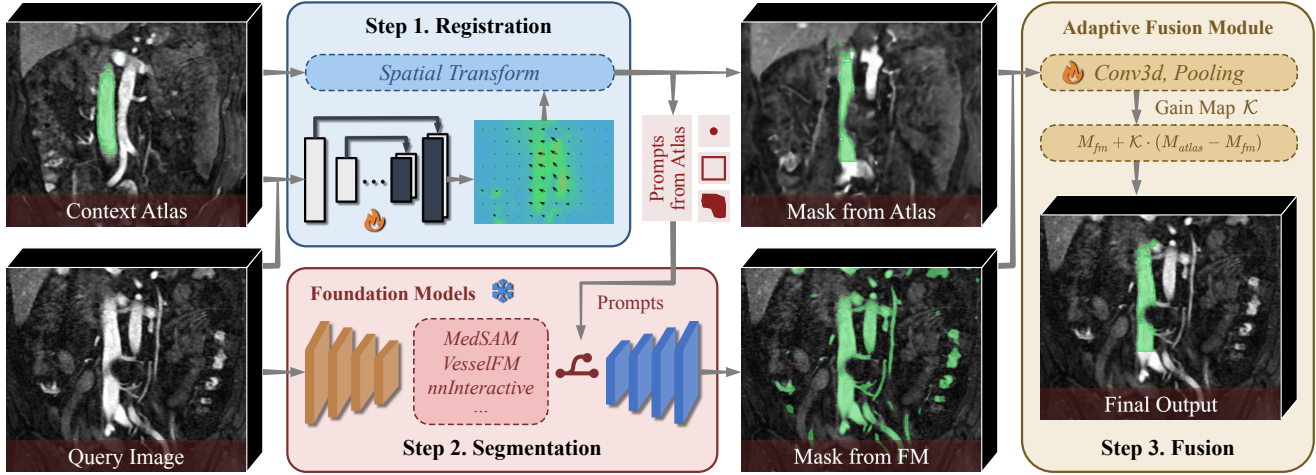


Figure 3. Pipeline including three steps: 1) Registration between query and support to obtain the mask (see Sec. 3.3), 2) Prompting the foundation model based on the mask from atlas (see Sec. 3.4), and 3) Fusion of the two masks to obtain the final result (see Sec. 3.5). Our model uses an inference-only design, where the ‘fire’ denotes test-time adaptation and the ‘snow’ remains frozen.

or depend on large pretrained encoders such as DINO [26] for feature extraction, limiting their practical clinical use. As in Fig. 3, we propose an atlas-guided, in-context segmentation framework that combines the strengths of classical atlas-based registration and advanced foundation models. AtlasSegFM consists of three steps: 1) atlas-based registration to provide context-aware prompts, 2) segmentation refinement using foundation models with these prompts, and 3) a fusion module to integrate predictions from both sources.

3.3. Registration and Prompt Generation

To generate task-specific prompts for foundation models, we adopt an atlas-based registration approach as the initialization step for in-context learning with two main advantages: 1) atlas-based registration does not require training or labeled datasets, making it lightweight and easy to deploy in clinical workflows, and 2) it inherently leverages structural priors, which are particularly valuable for medical image segmentation tasks where anatomical consistency is critical.

Traditional atlas-based segmentation relies on iterative optimization to align the atlas to the query image, which is computationally expensive and time-consuming. To overcome this, we develop a test-time registration network derived from VoxelMorph [1], utilizing its network architecture and optimization objectives with adaptations for test-time optimization. Formally, given a context atlas (X_{atlas}, Y_{atlas}) and a query image X_{query} , we estimate the spatial transformation T by optimizing:

$$T^* = \arg \min_T \mathcal{L}_{reg}(T(X_{atlas}), X_{query}) \quad (2)$$

where \mathcal{L}_{reg} is a similarity-based registration loss, such as normalized cross-correlation or mutual information. The registered atlas $T^* X_{atlas}$ and its corresponding label $T^* Y_{atlas}$

yield a coarse segmentation mask M_{atlas} , which serves as a structural prior.

Original VoxelMorph optimizes registration by training on large datasets to learn network parameters. In AtlasSegFM, we repurpose it as a test-time optimization framework, where the network parameters are optimized on-the-fly for each specific atlas-query pair during inference. In addition, we perform rigid and affine pre-registration prior to network optimization, ensuring coarse alignment and enhancing final registration accuracy (as validated in the ablation Table 4).

After generating the coarse segmentation mask M_{atlas} from the registered atlas, we adapt it as the prompt context for foundation models. Specifically, M_{atlas} is used to derive various forms of prompts:

- Click: The center of the largest connected region in M_{atlas} is extracted as the click location $Prompt_{click}$.
- Box: The minimum bounding box that encloses M_{atlas} is computed as the box prompt $Prompt_{box}$.
- Mask: The segmentation mask M_{atlas} itself is directly used as the mask prompt $Prompt_{mask}$.

These task-specific prompts fully utilize the structural prior provided by M_{atlas} , ensuring that the foundation models receive precise and anatomically relevant guidance. (more details can be found in Sec. 6 of the Supplementary Material)

3.4. Segmentation Foundation Models

To seamlessly integrate different foundation models, our pipeline is designed to accommodate both interactive and non-interactive architectures. With the prompt $Prompt_i$, where $i \in \text{click, box, mask}$, generated from the previous step, we use them whenever the chosen foundation model supports prompting to refine the segmentation.

Interactive foundation models require prompts to guide the segmentation process. In our pipeline, we provide various prompt types, allowing the model to select the most suitable prompt based on its capabilities. For domain-specific but non-interactive models such as vesselFM, the model instead operates directly on input images without prompts, leveraging its pretrained domain knowledge to produce segmentation.

This unified design allows our pipeline to adapt to different scenarios and leverage the strengths of both interactive and domain-specific foundation models. The foundation model output can be expressed as:

$$M_{fm} = f_{FM}(X_{query}, Prompt_i) \quad (3)$$

where f_{FM} represents the foundation model.

3.5. Atlas–FM Adaptive Fusion

Although the foundation model provides fine-grained segmentation M_{fm} , it may occasionally fail in ambiguous regions or under challenging scenarios. On the other hand, the atlas-based mask M_{atlas} offers robust structural priors but generally lacks fine detail. To address the limitations of both methods, we design a fusion module to dynamically integrate the predictions from the atlas and the foundation model, leveraging their complementary strengths.

The final mask M_{final} is computed by combining M_{atlas} and M_{fm} through a learnable Kalman filter:

$$M_{final} = M_{fm} + \mathcal{K} \cdot (M_{atlas} - M_{fm}) \quad (4)$$

where \mathcal{K} is the Kalman gain, which determines the contribution of the atlas-based mask to the final segmentation. Intuitively, \mathcal{K} assigns higher weight to M_{atlas} in regions where the foundation model is uncertain and vice versa.

Unlike a traditional Kalman filter where \mathcal{K} is computed based on fixed uncertainty estimates, we implement \mathcal{K} as a learnable component using a lightweight neural network. Specifically, \mathcal{K} is dynamically predicted based on the features of both M_{atlas} and M_{fm} by:

$$\mathcal{K} = \sigma(g([M_{atlas}, M_{fm}])) \quad (5)$$

where $g(\cdot)$ is a lightweight network composed of 3D convolutional layers and pooling operations, and $\sigma(\cdot)$ is the sigmoid activation function to ensure $\mathcal{K} \in [0, 1]$. In our experiment, the function $g(\cdot)$ is composed of three parallel 3D max-pooling operations with kernel sizes of 3, 5, and 7, and the pooled features are adaptively fused through learnable weights to capture multi-scale contextual information.

4. Experiments

4.1. Experimental Setup

Datasets. We evaluate our proposed method on six datasets, covering commonly used few-shot medical image segmentation tasks and clinically significant challenges:

- **Abd-CT** [16]: Abdominal CT dataset contains 30 CT scans with 4 annotated organ classes: liver, left kidney, right kidney, and spleen, treated as four contexts.
- **Abd-MR** [14]: Abdominal T2-SPIR MRI has 20 MRI scans with the same anatomy classes as Abd-CT, emphasizing inter-class ambiguity and modality challenges.
- **AVT** [28]: Aortic Vessel Tree contains 56 CTA scans for vascular segmentation with complex geometries.
- **Fe-MRA**: An in-house dataset of 50 ferumoxytol-enhanced MRA scans of the lower extremities, with arterial and venous structures annotated into 12 fine-grained categories such as the left/right great saphenous veins and femoral arteries. It targets lower-limb vasculature in clinical scenarios including diagnosis and treatment planning for varicose veins and arterial thrombosis.
- **OASIS** [9, 24]: It contains 414 MRI scans for brain segmentation, annotated for the major brain substructures.
- **BrainRT**: An in-house dataset of 60 CT/MR scans for brain tumor radiotherapy planning, where expert radiologists delineated organs-at-risk on CT and labels were registered to MR. It covers two crucial segmentation contexts: whole brain and organs-at-risk (eyes, optic nerves, optic chiasm, and brainstem), whose delineation is essential to minimize radiation-induced damage.

Protocol and metrics. Following [27], we adopt a 5-fold cross-validation protocol, where one sample from the remaining validation set is used as the context support for testing the query images in each fold. For datasets with multiple categories, each category is treated as a segmentation context. Four metrics are used: **1**) Dice measuring the overlap between the prediction and ground truth; **2**) NSD (Normalized Surface Dice) measuring the agreement between two surfaces within a specified tolerance; **3**) HD (Hausdorff Distance 95) quantifying the boundary error by computing the 95th percentile of the Hausdorff distance, lower better; **4**) cIDice (centerline Dice) emphasizing the correctness of the centerline connectivity, especially suitable for vessel.

Baselines. We compare our method against three categories: **1**) Supervised learning methods [6, 12] directly trained on the target dataset; **2**) Few-shot learning methods [4, 17, 27, 33] trained on the target dataset using annotations from other categories (e.g., training on liver and testing on spleen, and vice versa); **3**) In-context learning methods [1–3, 25, 27, 29, 37, 49, 50] that do not require training or fine-tuning on the target dataset, relying on general-purpose pretrained models or inference-time adaptation.

Implementation details. Our method consists of two learnable components, which are test-time optimized: **1**) Atlas-registration module. Derived from VoxelMorph [1], we use a lightweight 5-layer U-Net with 32 channels, optimized between support and query images using image similarity MSE loss with a learning rate of 1e-4 for 1000 iterations. **2**) Adaptive fusion module. It is optimized using the support

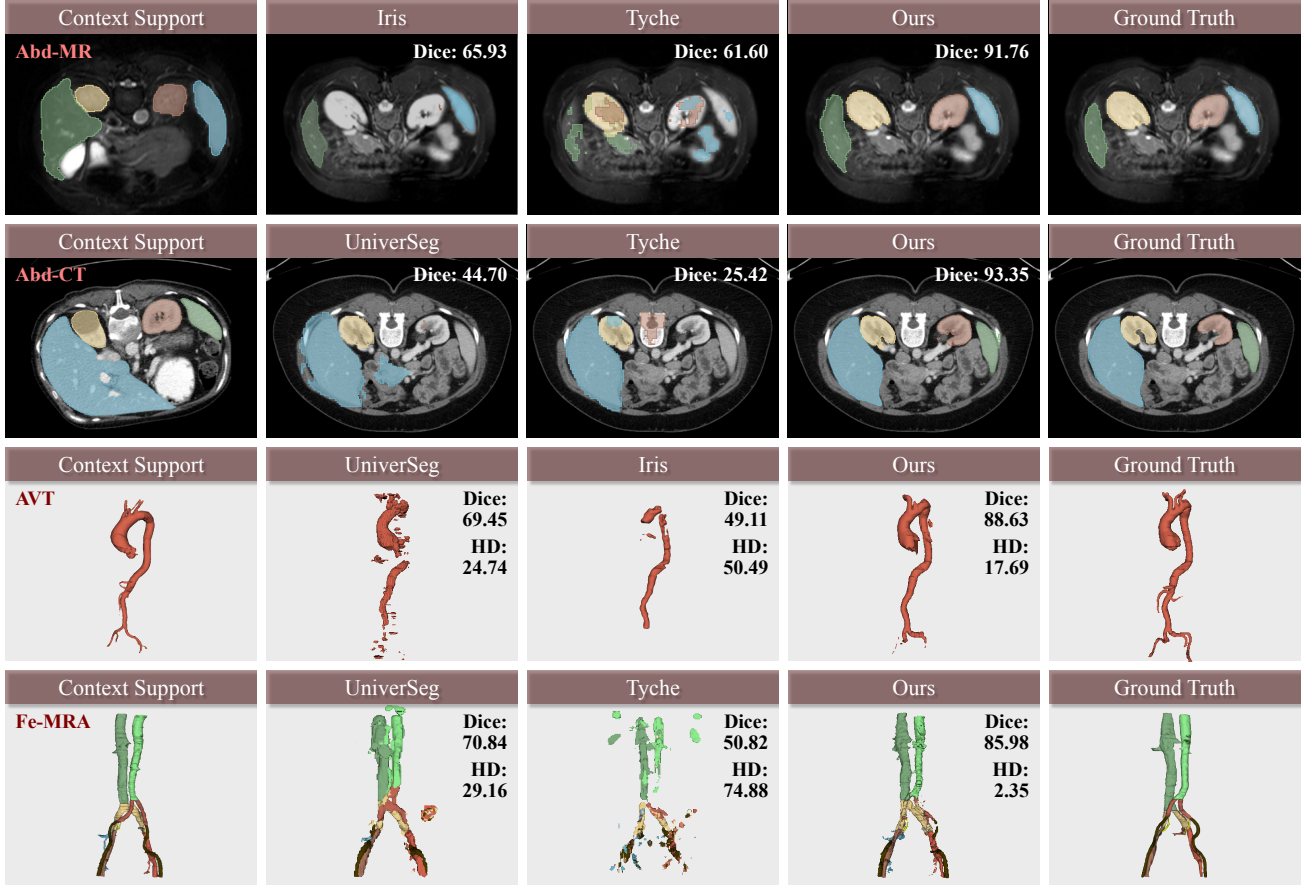


Figure 4. Visual comparisons against recent one-shot learning methods with open-source implementations (i.e., UniverSeg [3], Tyche [29], and Iris [6]) across four datasets. Each color corresponds to a specific context, and all contexts are combined in the visualization.

label with a Dice loss for segmentation, applying a learning rate of 1e-5 for 100 iterations. Both modules are optimized directly on the atlas-query pairs during test time, requiring no additional training dataset. For vascular segmentation, a recent foundation model vesselFM [38] is adopted, whereas nnInteractive [13] is applied to other scenarios using mask-based prompts.

4.2. Comparisons with State-of-the-art

Results on abdomen datasets. Table 1 summarizes the Dice score comparisons across different methods on the Abd-MR and Abd-CT datasets, focusing on the segmentation of multiple organs, including the liver, left kidney (LK), right kidney (RK), and spleen. Our method achieves the highest mean Dice scores on both datasets, with 81.22% on Abd-MR and 72.91% on Abd-CT, outperforming all baseline methods. Our approach achieves substantial performance gains over ICL methods, improving the mean Dice score on Abd-CT by 5.45% compared to MAUP [49] and 37.65% compared to Tyche [29], highlighting its robust generalization and adaptability across diverse scenarios. Even compared to super-

vised learning methods, our approach achieves competitive performance, delivering segmentation quality comparable to nnUNet [12], which relies on full supervision and target-specific training. This highlights the effectiveness of our method in achieving high-quality segmentation without the need for extensive labeled data.

Qualitative results in Fig. 4 (first two rows) further validate our method’s capability to produce segmentations with clear boundaries and fine structural details. In contrast, others often struggle with incomplete or inconsistent outputs due to limited structural priors or contextual information.

Results on brain datasets. Table 2 reports segmentation performance on the OASIS and BrainRT datasets, where our method achieves the highest Dice and NSD scores across all tasks. For whole-brain segmentation, while most methods achieve reasonable performance, our approach stands out by delivering the highest accuracy with consistently smooth and anatomically precise segmentations, achieving a 3.41 HD on the OASIS dataset. On the BrainRT dataset, which focuses on clinically significant organs-at-risk (e.g., optic nerves and brainstem), our method achieves a Dice score of

Table 1. Dice score comparisons of abdomen organ segmentation performance on the Abd-MR and Abd-CT datasets.

Methods	Reference	Abd-MR					Abd-CT				
		Liver	LK	RK	Spleen	Mean	Liver	LK	RK	Spleen	Mean
▼ Supervised with Target Dataset (80% Training, 20% Testing)											
nnUNet [31]	Nat. Methods 2021	92.02	92.09	92.74	89.38	91.56	95.57	86.75	89.39	90.83	90.64
Iris ^{1,*} [6]	CVPR 2025	88.77	33.13	55.66	75.19	63.19	94.52	91.66	93.00	93.55	93.18
▼ Finetuned with Other Categories on Target Dataset											
SSL-ALP [†] [27]	TMI 2022	70.49	81.25	79.86	64.49	74.02	67.29	76.35	72.62	70.11	71.59
CAT-Net [†] [17]	MICCAI 2023	73.01	73.11	79.54	69.31	73.73	66.24	69.09	47.83	66.98	62.54
GMRD [†] [4]	TMI 2024	73.65	75.97	89.95	65.44	76.25	63.06	79.92	62.27	56.48	65.43
DSPNet [†] [33]	MedIA 2025	75.06	81.88	85.37	70.93	78.31	69.32	78.01	74.54	69.31	72.79
▼ No Finetuning Required on Target Dataset											
VM-Base ^{2,*} [1]	TMI 2019	72.85	72.75	70.77	64.49	70.21	77.51	48.59	48.18	60.03	58.58
SSL-ALP [‡] [27]	TMI 2022	70.74	55.49	67.43	58.93	63.01	71.38	34.48	32.32	51.67	47.46
RPT [‡] [50]	MICCAI 2023	49.22	42.45	47.14	48.84	46.91	65.87	40.07	35.97	51.22	48.28
SegGPT [*] [37]	ICCV 2023	71.86	18.33	17.34	10.57	29.52	74.64	3.61	11.70	1.03	22.74
UniverSeg [*] [3]	ICCV 2023	67.27	58.80	47.83	39.16	53.27	77.36	32.45	46.28	36.61	48.17
IFA [‡] [25]	CVPR 2024	50.22	35.99	34.00	42.21	40.61	46.92	25.13	26.56	24.85	30.79
Tyche [*] [29]	CVPR 2024	61.20	51.37	77.92	40.56	57.76	68.78	18.16	38.53	15.59	35.26
FAMNet [‡] [2]	AAAI 2025	73.01	57.28	74.68	58.21	65.79	73.57	57.79	61.89	65.78	64.75
MAUP [‡] [49]	MICCAI 2025	78.16	58.23	72.34	59.65	67.09	78.25	59.41	71.80	60.38	67.46
Ours		83.77	81.11	83.54	77.83	81.22	90.06	63.27	62.50	75.79	72.91

¹Iris is designed for one-shot in-context learning, but it uses Abd-MR/Abd-CT for training and is thus categorized under the supervised group.

²Using VoxelMorph to estimate the deformation field from the support to the query and apply it to the mask.

*Reproduced using public code or our reimplementation under the 1-shot protocol. [†]Cited from DSPNet [33]. [‡]Cited from MAUP [49].

77.07% and an NSD of 77.55%, significantly outperforming all baselines. Accurate segmentation of these structures is crucial in radiotherapy to minimize severe radiation-induced damage; however, even the state-of-the-art Iris method struggles with unseen structures, underscoring the importance and difficulty of this task. As shown in Fig. 2, foundation models (e.g., nnInteractive 1/5 clicks) perform poorly or even fail on organs-at-risk segmentation due to the intricate structures and small size of these regions, which demand finer detail preservation and better contextual understanding.

Results on vessel datasets. In Table 3, we evaluate on vessel segmentation, a challenging task due to intricate geometries and thin structures. Our method achieves the highest Dice scores (71.56% on AVT and 84.42% on Fe-MRA) and cIDice scores (59.91% on AVT and 82.99% on Fe-MRA), while significantly outperforming other methods in HD (39.23 on AVT and 3.00 on Fe-MRA). These results demonstrate its capability to accurately capture complex vascular structures and maintain smooth, anatomically consistent surfaces.

As shown in Fig. 4 (last 2 rows), our method reconstructs the full topology of the aortic vessel tree on AVT and clearly delineates both arterial and venous structures on Fe-MRA, outperforming other methods that struggle with incomplete outputs. This highlights our method’s ability to produce detailed, anatomically consistent segmentations.

4.3. Ablation Studies

Table 4 shows the ablation studies, where we evaluate the impact of different modules in our framework on the Abd-MR and Fe-MRA datasets. This analysis highlights the contributions of atlas-based registration, pre-registration strategies, foundation model prompts, and the fusion module.

Atlas-FM registration. The performance of Baseline #1, which uses only atlas-based registration, sets the starting point for analysis. By simply aligning between atlas and query, the Dice scores are achieved as 43.77% on Abd-MR and 35.73% on Fe-MRA. Pre-registration also improves the performance. Specifically, introducing rigid pre-registration raises Dice scores to 60.29% on Abd-MR and 66.43% on Fe-MRA. Further incorporating affine pre-registration to better account for anatomical variations boosts performance to 70.21% and 81.64% on Abd-MR and Fe-MRA.

Foundation models. Baseline #2 evaluates the independent performance of the foundation model. For Abd-MR, when we prompt nnInteractive with one point per image, the Dice score is 51.82%. On Fe-MRA, vesselFM achieves a Dice score of 55.28%, leveraging its pre-trained capabilities for fine-grained segmentation. By providing atlas-derived prompts to the foundation model, the performance on Abd-MR increases to 69.13%, showcasing the utility of structural priors in guiding the foundation model.

Table 2. Comparisons of the brain-structure and organs-at-risk segmentation performance on the OASIS and BrainRT datasets. nn: nnInteractive.

Methods	OASIS		BrainRT					
			Whole-brain			Organs-at-risk		
	Dice \uparrow	HD \downarrow	Dice \uparrow	NSD \uparrow	HD \downarrow	Dice \uparrow	NSD \uparrow	HD \downarrow
▼ Foundation Models (1 or 5 clicks per test image)								
nn-1	16.41	36.22	0.62	1.82	104.04	30.65	24.38	90.01
nn-5	59.43	6.32	61.63	40.31	27.62	39.09	26.42	59.63
▼ In-context Models (One support each context)								
SegGPT	22.34	42.13	50.60	58.13	19.38	-	-	-
UniverSeg	81.21	12.70	83.32	32.44	15.40	0.39	3.83	32.59
Tyche	80.45	8.96	88.96	47.10	14.69	4.37	10.03	38.76
Iris	41.11	14.44	-	-	-	-	-	-
Ours	85.08	3.41	91.24	63.08	6.78	77.07	77.55	5.17

Table 4. Ablation with incremental addition of modules.

Module settings	Abd-MR	Fe-MRA
Baseline #1 (Atlas registration)	43.77	35.73
+ Rigid pre-registration	60.29	66.43
+ Affine pre-registration	70.21	81.64
Baseline #2 (Foundation model)	51.82*	55.28
+ Prompts from atlas	69.13	N/A [†]
+ Adaptive fusion (Final)	81.22	84.42

*One point prompt is additionally provided to obtain this result.

[†]The foundation model used for Fe-MRA, vesselFM, is not promptable.

Table 5. Comparison of inference time and learnable parameters.

Methods	Inference Time	Learnable Param.
SegGPT	18.1 min/image	1.4G
UniverSeg	2.2 min/image	1.2M
Tyche	2.1 min/image	1.2M
Ours (Total)	1.8 min/image	1.4M
- Registration	1.5 min/image	1.3M
- Foundation model	0.01 min/image	-
- Fusion	0.3 min/image	0.1M

Atlas-FM fusion. Atlas registration provides accurate global structure, whereas foundation models demonstrate better local details. As listed in the last row, our adaptive fusion module combines the registered atlas prediction and the foundation model prediction, achieving Dice scores of 81.22% on Abd-MR and 84.42% on Fe-MRA, surpassing either prediction alone and demonstrating the benefit of fusing their complementary strengths.

Runtime and parameter efficiency. Table 5 measures the computational cost on NVIDIA RTX4090 GPU using a (256 \times 256 \times 240) image from the BrainRT organs-at-risk task. Unlike slice-by-slice methods such as SegGPT, Tyche, and UniverSeg, which reconstruct 3D volumes by sequentially processing 2D slices, our method operates directly on

Table 3. Comparisons of the vessel segmentation performance on the AVT and Fe-MRA datasets. nn: nnInteractive.

Methods	AVT			Fe-MRA		
	Dice \uparrow	clDice \uparrow	HD \downarrow	Dice \uparrow	clDice \uparrow	HD \downarrow
▼ Foundation Models (1 or 5 clicks per test image)						
vesselFM	28.19	7.11	274.02	60.31	41.74	124.34
nn-1	63.31	53.27	65.79	43.69	23.12	182.87
nn-5	83.38	70.52	43.69	49.36	34.00	110.01
▼ In-context Models (One support each context)						
SegGPT	68.73	48.78	45.05	0.31	0.69	133.15
UniverSeg	39.71	31.89	51.12	69.71	53.20	39.61
Tyche	53.24	42.76	70.44	50.21	59.64	79.28
Iris	45.44	41.93	58.53	28.35	13.66	38.88
Ours	71.56	59.91	39.23	84.42	82.99	3.00

the full 3D image. This enables faster inference, taking 1.8 minutes per image compared to 18.1 minutes for SegGPT and 2.2 minutes for Tyche and UniverSeg.

The inference time is further broken down by stage: atlas-based registration requires 1.5 minutes for alignment, the fusion module integrates predictions in 0.3 minutes, and the foundation model completes inference in just 0.01 minutes. With only 1.4M learnable parameters and a single support-query pair for test-time adaptation, our method is lightweight, practical, and demonstrates relatively higher efficiency.

5. Conclusion

In this paper, we introduced AtlasSegFM, a simple yet effective medical image segmentation framework. By leveraging the globally consistent structure provided by the atlas and the representation power of foundation models, AtlasSegFM fuses their complementary strengths and achieves state-of-the-art performance. AtlasSegFM offers the following advantages: **1)** It fully exploits off-the-shelf foundation models, enabling context-specific customization with a single atlas and no additional training data. **2)** Experiments across six datasets demonstrate an average Dice of 80.72%, substantially outperforming both uncustomized foundation models and existing in-context learning methods. **3)** In uncommon contexts underrepresented in foundation model pretraining, such as organs-at-risk, our method achieves a Dice of 77.07% without training on similar cases, demonstrating strong out-of-distribution robustness for small, delicate structures.

Limitations and future direction. While effective for organ segmentation, our method is less suitable for lesion segmentation due to the dependence on structural consistency between support and query images, which focal lesions often lack. It also faces challenges with patients whose anatomy differs markedly from the atlas. Future work will explore multi-atlas strategies for greater robustness and refine prompt generation for more context-aware guidance.

References

[1] Guha Balakrishnan, Amy Zhao, Mert R Sabuncu, John Guttag, and Adrian V Dalca. Voxelmorph: a learning framework for deformable medical image registration. *IEEE Transactions on Medical Imaging*, 38(8):1788–1800, 2019. [3](#), [4](#), [5](#), [7](#)

[2] Yuntian Bo, Yazhou Zhu, Lunbo Li, and Haofeng Zhang. Famnet: Frequency-aware matching network for cross-domain few-shot medical image segmentation. In *AAAI*, pages 1889–1897, 2025. [7](#)

[3] Victor Ion Butoi, Jose Javier Gonzalez Ortiz, Tianyu Ma, Mert R Sabuncu, John Guttag, and Adrian V Dalca. Universeg: Universal medical image segmentation. In *ICCV*, pages 21438–21451, 2023. [2](#), [3](#), [5](#), [6](#), [7](#)

[4] Ziming Cheng, Shidong Wang, Tong Xin, Tao Zhou, Haofeng Zhang, and Ling Shao. Few-shot medical image segmentation via generating multiple representative descriptors. *IEEE Transactions on Medical Imaging*, 43(6):2202–2214, 2024. [3](#), [5](#), [7](#)

[5] Yunhe Gao, Mu Zhou, and Dimitris N Metaxas. Utnet: a hybrid transformer architecture for medical image segmentation. In *MICCAI*, pages 61–71, 2021. [2](#)

[6] Yunhe Gao, Di Liu, Zhuowei Li, Yunsheng Li, Dongdong Chen, Mu Zhou, and Dimitris N Metaxas. Show and segment: Universal medical image segmentation via in-context learning. In *CVPR*, pages 20830–20840, 2025. [2](#), [3](#), [5](#), [6](#), [7](#)

[7] Shizhan Gong, Yuan Zhong, Wenao Ma, Jinpeng Li, Zhao Wang, Jingyang Zhang, Pheng-Ann Heng, and Qi Dou. 3dsam-adapter: Holistic adaptation of sam from 2d to 3d for promptable tumor segmentation. *Medical Image Analysis*, 98:103324, 2024. [3](#)

[8] Malte Hoffmann, Benjamin Billot, Douglas N Greve, Juan Eugenio Iglesias, Bruce Fischl, and Adrian V Dalca. Synthmorph: learning contrast-invariant registration without acquired images. *IEEE Transactions on Medical Imaging*, 41(3):543–558, 2021. [3](#)

[9] Andrew Hoopes, Malte Hoffmann, Douglas N Greve, Bruce Fischl, John Guttag, and Adrian V Dalca. Learning the effect of registration hyperparameters with hypermorph. *The Journal of Machine Learning for Biomedical Imaging*, 1:003, 2022. [5](#)

[10] Jiesi Hu, Yang Shang, Yanwu Yang, Xutao Guo, Hanyang Peng, and Ting Ma. Icl-sam: Synergizing in-context learning model and sam in medical image segmentation. In *MIDL*, pages 641–656, 2024. [3](#)

[11] Juan Eugenio Iglesias and Mert R Sabuncu. Multi-atlas segmentation of biomedical images: a survey. *Medical Image Analysis*, 24(1):205–219, 2015. [3](#)

[12] Fabian Isensee, Paul F Jaeger, Simon AA Kohl, Jens Petersen, and Klaus H Maier-Hein. nnu-net: a self-configuring method for deep learning-based biomedical image segmentation. *Nature Methods*, 18(2):203–211, 2021. [3](#), [5](#), [6](#)

[13] Fabian Isensee, Maximilian Rokuss, Lars Krämer, Stefan Dinkelacker, Ashis Ravindran, Florian Stritzke, Benjamin Hamm, Tassilo Wald, Moritz Langenberg, Constantin Ulrich, et al. nninteractive: Redefining 3d promptable segmentation. *arXiv preprint arXiv:2503.08373*, 2025. [1](#), [2](#), [3](#), [6](#)

[14] A Emre Kavur, N Sinem Gezer, Mustafa Barış, Sinem Aslan, Pierre-Henri Conze, Vladimir Groza, Duc Duy Pham, Soumick Chatterjee, Philipp Ernst, Savaş Özkan, et al. Chaos challenge-combined (ct-mr) healthy abdominal organ segmentation. *Medical Image Analysis*, 69:101950, 2021. [5](#)

[15] Alexander Kirillov, Eric Mintun, Nikhila Ravi, Hanzi Mao, Chloe Rolland, Laura Gustafson, Tete Xiao, Spencer Whitehead, Alexander C Berg, Wan-Yen Lo, et al. Segment anything. In *ICCV*, pages 4015–4026, 2023. [1](#), [3](#)

[16] Bennett Landman, Zhoubing Xu, Juan Iglesias, Martin Styner, Thomas Langerak, and Arno Klein. Miccai multi-atlas labeling beyond the cranial vault—workshop and challenge. In *MICCAI workshop*, page 12, 2015. [5](#), [3](#)

[17] Yi Lin, Yufan Chen, Kwang-Ting Cheng, and Hao Chen. Few shot medical image segmentation with cross attention transformer. In *MICCAI*, pages 233–243, 2023. [3](#), [5](#), [7](#)

[18] Jiarun Liu, Hao Yang, Hong-Yu Zhou, Lequan Yu, Yong Liang, Yizhou Yu, Shaoting Zhang, Hairong Zheng, and Shanshan Wang. Swin-umamba[†]: Adapting mamba-based vision foundation models for medical image segmentation. *IEEE Transactions on Medical Imaging*, 2024. [2](#)

[19] Yang Liu, Muzhi Zhu, Hao Chen, Xinlong Wang, Bo Feng, Hao Wang, Shiyu Li, Raviteja Vemulapalli, and Chunhua Shen. Segment anything in context with vision foundation models. *International Journal of Computer Vision*, 133(10):7460–7485, 2025. [3](#)

[20] Jinxin Lv, Xiaoyu Zeng, Sheng Wang, Ran Duan, Zhiwei Wang, and Qiang Li. Robust one-shot segmentation of brain tissues via image-aligned style transformation. In *AAAI*, pages 1861–1869, 2023. [3](#)

[21] Jun Ma, Yuting He, Feifei Li, Lin Han, Chenyu You, and Bo Wang. Segment anything in medical images. *Nature Communications*, 15(1):654, 2024. [1](#), [2](#), [3](#)

[22] Jun Ma, Zongxin Yang, Sumin Kim, Bihui Chen, Mohammed Baharoon, Adibvafa Fallahpour, Reza Asakereh, Hongwei Lyu, and Bo Wang. Medsam2: Segment anything in 3d medical images and videos. *arXiv preprint arXiv:2504.03600*, 2025. [1](#), [3](#)

[23] Xinyu Mao, Xiaohan Xing, Fei Meng, Jianbang Liu, Fan Bai, Qiang Nie, and Max Meng. One polyp identifies all: One-shot polyp segmentation with sam via cascaded priors and iterative prompt evolution. In *ICCV*, pages 24182–24191, 2025. [3](#)

[24] Daniel S Marcus, Tracy H Wang, Jamie Parker, John G Csernansky, John C Morris, and Randy L Buckner. Open access series of imaging studies (oasis): cross-sectional mri data in young, middle aged, nondemented, and demented older adults. *Journal of Cognitive Neuroscience*, 19(9):1498–1507, 2007. [5](#)

[25] Jiahao Nie, Yun Xing, Gongjie Zhang, Pei Yan, Aoran Xiao, Yap-Peng Tan, Alex C Kot, and Shijian Lu. Cross-domain few-shot segmentation via iterative support-query correspondence mining. In *CVPR*, pages 3380–3390, 2024. [5](#), [7](#)

[26] Maxime Oquab, Timothée Darcret, Théo Moutakanni, Huy Vo, Marc Szafraniec, Vasil Khalidov, Pierre Fernandez, Daniel Haziza, Francisco Massa, Alaaeldin El-Nouby, et al. Dinov2: Learning robust visual features without supervision. *arXiv preprint arXiv:2304.07193*, 2023. [4](#)

[27] Cheng Ouyang, Carlo Biffi, Chen Chen, Turkay Kart, Huaqi Qiu, and Daniel Rueckert. Self-supervised learning for few-shot medical image segmentation. *IEEE Transactions on Medical Imaging*, 41(7):1837–1848, 2022. 3, 5, 7

[28] Lukas Radl, Yuan Jin, Antonio Pepe, Jianning Li, Christina Gsaxner, Fen-hua Zhao, and Jan Egger. Avt: Multicenter aortic vessel tree cta dataset collection with ground truth segmentation masks. *Data in Brief*, 40:107801, 2022. 5, 3

[29] Marianne Rakic, Hallee E Wong, Jose Javier Gonzalez Ortiz, Beth A Cimini, John V Guttag, and Adrian V Dalca. Tyche: Stochastic in-context learning for medical image segmentation. In *CVPR*, pages 11159–11173, 2024. 2, 5, 6, 7, 3

[30] Nikhila Ravi, Valentin Gabeur, Yuan-Ting Hu, Ronghang Hu, Chaitanya Ryali, Tengyu Ma, Haitham Khedr, Roman Rädle, Chloe Rolland, Laura Gustafson, et al. Sam 2: Segment anything in images and videos. *arXiv preprint arXiv:2408.00714*, 2024. 1, 3

[31] Olaf Ronneberger, Philipp Fischer, and Thomas Brox. U-net: Convolutional networks for biomedical image segmentation. In *MICCAI*, pages 234–241, 2015. 2, 7

[32] Jiacheng Ruan, Jincheng Li, and Suncheng Xiang. Vm-unet: Vision mamba unet for medical image segmentation. *ACM Transactions on Multimedia Computing, Communications and Applications*, 2024. 2

[33] Song Tang, Shaxu Yan, Xiaozhi Qi, Jianxin Gao, Mao Ye, Jianwei Zhang, and Xiatian Zhu. Few-shot medical image segmentation with high-fidelity prototypes. *Medical Image Analysis*, 100:103412, 2025. 3, 5, 7

[34] Hongzhi Wang, Jung W Suh, Sandhitsu R Das, John B Pluta, Caryne Craige, and Paul A Yushkevich. Multi-atlas segmentation with joint label fusion. *IEEE Transactions on Pattern Analysis and Machine Intelligence*, 35(3):611–623, 2012. 3

[35] Hongyi Wang, Shiao Xie, Lanfen Lin, Yutaro Iwamoto, Xian-Hua Han, Yen-Wei Chen, and Ruofeng Tong. Mixed transformer u-net for medical image segmentation. In *ICASSP*, pages 2390–2394, 2022. 2

[36] Haoyu Wang, Sizheng Guo, Jin Ye, Zhongying Deng, Junlong Cheng, Tianbin Li, Jianpin Chen, Yanzhou Su, Ziyuan Huang, Yiqing Shen, et al. Sam-med3d: A vision foundation model for general-purpose segmentation on volumetric medical images. *IEEE Transactions on Neural Networks and Learning Systems*, 2025. 3

[37] Xinlong Wang, Xiaosong Zhang, Yue Cao, Wen Wang, Chunhua Shen, and Tiejun Huang. Seggpt: Towards segmenting everything in context. In *CVPR*, pages 1130–1140, 2023. 2, 5, 7

[38] Bastian Wittmann, Yannick Wattenberg, Tamaz Amiranashvili, Suprosanna Shit, and Bjoern Menze. vesselfm: A foundation model for universal 3d blood vessel segmentation. In *CVPR*, pages 20874–20884, 2025. 3, 6

[39] Hallee E Wong, Marianne Rakic, John Guttag, and Adrian V Dalca. Scribbleprompt: fast and flexible interactive segmentation for any biomedical image. In *ECCV*, pages 207–229, 2024. 1, 3

[40] Hallee E Wong, Jose Javier Gonzalez Ortiz, John Guttag, and Adrian V Dalca. Multiverseg: Scalable interactive segmentation of biomedical imaging datasets with in-context guidance. In *ICCV*, pages 20966–20980, 2025. 1, 3

[41] Junde Wu and Min Xu. One-prompt to segment all medical images. In *CVPR*, pages 11302–11312, 2024.

[42] Shiao Xie, Liangjun Zhang, Ziwei Niu, Fanfan Ye, Qiaoyong Zhong, Di Xie, Yen-Wei Chen, and Lanfen Lin. Eicseg: Universal medical image segmentation via explicit in-context learning. *IEEE Transactions on Medical Imaging*, 2025. 3

[43] Zhaohu Xing, Tian Ye, Yijun Yang, Guang Liu, and Lei Zhu. Segmamba: Long-range sequential modeling mamba for 3d medical image segmentation. In *MICCAI*, pages 578–588, 2024. 2

[44] Qianxiong Xu, Lanyun Zhu, Xuanyi Liu, Guosheng Lin, Cheng Long, Ziyue Li, and Rui Zhao. Unlocking the power of sam 2 for few-shot segmentation. In *ICML*, 2025. 3

[45] Xuzhe Zhang, Yuhao Wu, Elsa Angelini, Ang Li, Jia Guo, Jerod M Rasmussen, Thomas G O’Connor, Pathik D Wadhwa, Andrea Parolin Jackowski, Hai Li, et al. Mapseg: Unified unsupervised domain adaptation for heterogeneous medical image segmentation based on 3d masked autoencoding and pseudo-labeling. In *CVPR*, pages 5851–5862, 2024. 3

[46] Jianwei Zhao, Fan Yang, Xin Li, Zicheng Jiao, Qiang Zhai, Xiaomeng Li, De Wu, Huazhu Fu, and Hong Cheng. Segmic: A universal model for medical image segmentation through in-context learning. *Pattern Recognition*, page 112179, 2025. 3

[47] Hong-Yu Zhou, Jiansen Guo, Yinghao Zhang, Xiaoguang Han, Lequan Yu, Liansheng Wang, and Yizhou Yu. nn-former: Volumetric medical image segmentation via a 3d transformer. *IEEE Transactions on Image Processing*, 32: 4036–4045, 2023. 2

[48] Zongwei Zhou, Md Mahfuzur Rahman Siddiquee, Nima Tajbakhsh, and Jianming Liang. Unet++: Redesigning skip connections to exploit multiscale features in image segmentation. *IEEE Transactions on Medical Imaging*, 39(6):1856–1867, 2019. 2

[49] Yazhou Zhu and Haofeng Zhang. Maup: Training-free multi-center adaptive uncertainty-aware prompting for cross-domain few-shot medical image segmentation. In *MICCAI*, pages 326–336, 2025. 3, 5, 6, 7

[50] Yazhou Zhu, Shidong Wang, Tong Xin, and Haofeng Zhang. Few-shot medical image segmentation via a region-enhanced prototypical transformer. In *MICCAI*, pages 271–280, 2023. 5, 7

Atlas is Your Perfect Context: One-Shot Customization for Generalizable Foundational Medical Image Segmentation

Supplementary Material

6. Prompt Engineering and Selection Strategy

A critical component of our proposed AtlasSegFM framework is the translation of the coarse structural prior provided by the registered atlas into an effective prompt for the Foundation Models. Different FMs exhibit varying sensitivities to prompt types (e.g., points, boxes, or dense masks) based on their pretraining objectives and architecture. We conducted a systematic ablation study to determine the optimal prompting strategy for two distinct foundation models: nnInteractive [13] and the MedSAM2 [22].

Prompt Generation. Based on the coarse mask M_{atlas} obtained from the registration step, we generate three types of prompts:

- Click: The center of the largest connected component in M_{atlas} .
- Box: The minimum bounding box enclosing M_{atlas} .
- Mask: The dense voxel-wise mask M_{atlas} itself.

Following the inference protocols of nnInteractive and MedSAM2, point and box prompts are provided on one slice. Specifically, we derive the 2D bounding box from the middle slice of M_{atlas} . nnInteractive utilizes this input to directly infer the 3D volume, whereas MedSAM2 initiates segmentation at the middle slice and propagates the prediction bidirectionally through the volume.

Selection for nnInteractive. As shown in Table 6, nnInteractive benefits significantly from dense semantic guidance. Since nnInteractive was designed to refine segmentation iteratively based on user interactions (which are essentially sparse masks), it generalizes exceptionally well when provided with the full Atlas Mask as the initial input. Using the Mask prompt yields the highest Dice score of 72.91% on the Abd-CT dataset, slightly outperforming the Box prompt (72.73%) and significantly surpassing the Point prompt (65.68%). This superiority is further corroborated by the boundary metrics, where the Mask prompt achieves the lowest HD95 of 27.52, indicating better shape conformity. Consequently, we utilize the Mask as the default prompt for nnInteractive in our main pipeline.

To demonstrate the effectiveness of our atlas-guided prompting strategy, we visualize the segmentation results of nnInteractive under different prompt types in Fig. 5. While our method successfully generates effective Click and Box prompts that yield competitive results, the Mask prompt consistently achieves the optimal segmentation performance. For the Spleen, although the Click (97.43%) and Box (97.49%) prompts provide strong guidance, the Mask prompt further refines the result, reaching the highest Dice

Table 6. Prompt-type ablation for atlas-guided prompting on Abd-CT using different foundation models. We compare three atlas-derived prompts (Click, Box, Mask) in AtlasSegFM for nnInteractive and MedSAM2.

Foundation Model	Prompt Type	Dice	HD95
nnInteractive	Click	65.68	36.19
	Box	72.73	30.35
	Mask	72.91	27.52
MedSAM2	Click	71.64	26.15
	Box	66.65	28.98
	Mask	69.49	25.63

score of 97.86%. This indicates that the dense spatial information provided by the atlas mask offers the most precise guidance for the model. In the case of the Liver, a similar trend is observed where the Mask prompt (92.90%) provides a robust segmentation that captures the complex organ shape effectively. These results validate that while our AtlasSegFM framework is versatile enough to generate various valid prompts, utilizing the Mask as the prompt maximizes the potential of nnInteractive, providing the most detailed structural priors for accurate segmentation.

Selection for MedSAM2. In contrast to nnInteractive, MedSAM2 exhibits a preference for simpler geometric prompts over dense masks or bounding boxes when initialized from a coarse atlas. As detailed in Table 6, the Click prompt achieves the best performance with a Dice score of 71.64%, outperforming the Mask (69.49%) and the Box (66.65%). Although the Mask prompt yields a slightly lower HD95 (25.63 vs. 26.15 for Click), the Click prompt offers a superior balance of overlap accuracy and geometric simplicity. This suggests that for MedSAM2’s propagation mechanism, a precise click derived from the centroid serves as a robust anchor, whereas a coarse bounding box or a noisy dense mask might introduce restrictive priors that hinder the model’s ability to propagate accurate predictions across slices. Therefore, we adopt the Click prompt strategy for the MedSAM2 branch of our framework.

Failure cases of our method on the Abd-CT and AVT datasets. In contrast to nnInteractive, the MedSAM2 model exhibits a distinct preference for sparse prompt guidance generated by our atlas. As shown in Fig. 6, we visualize the segmentation performance across different prompt types. For the Spleen, the Click prompt yields the most accurate segmentation with a Dice score of 96.59%, successfully capturing the organ’s boundary. Conversely, the Box prompt

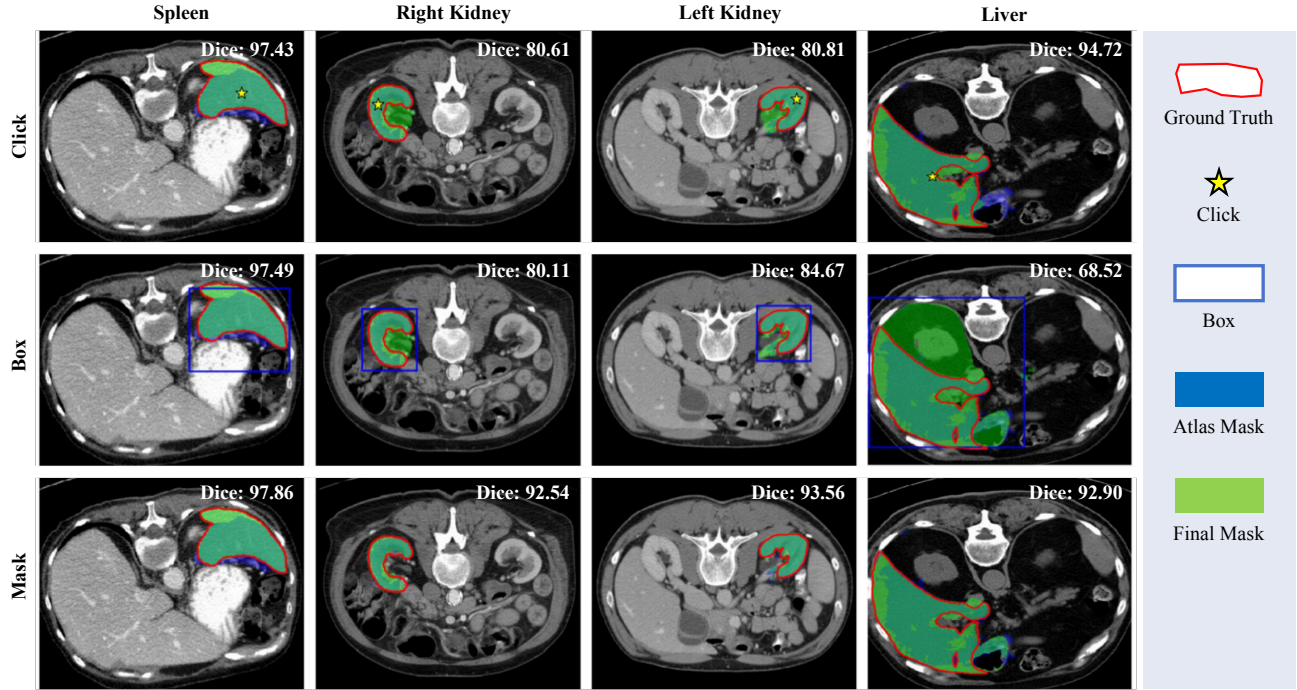


Figure 5. Qualitative results of AtlasSegFM with nnInteractive using atlas-derived prompts on Abd-CT. Rows indicate prompt type (Click / Box / Mask); columns show Spleen, Right Kidney, Left Kidney, and Liver. Dice is reported per case. The Mask prompt is the most robust, particularly for challenging targets such as kidneys by providing a dense structural prior beyond coarse localization.

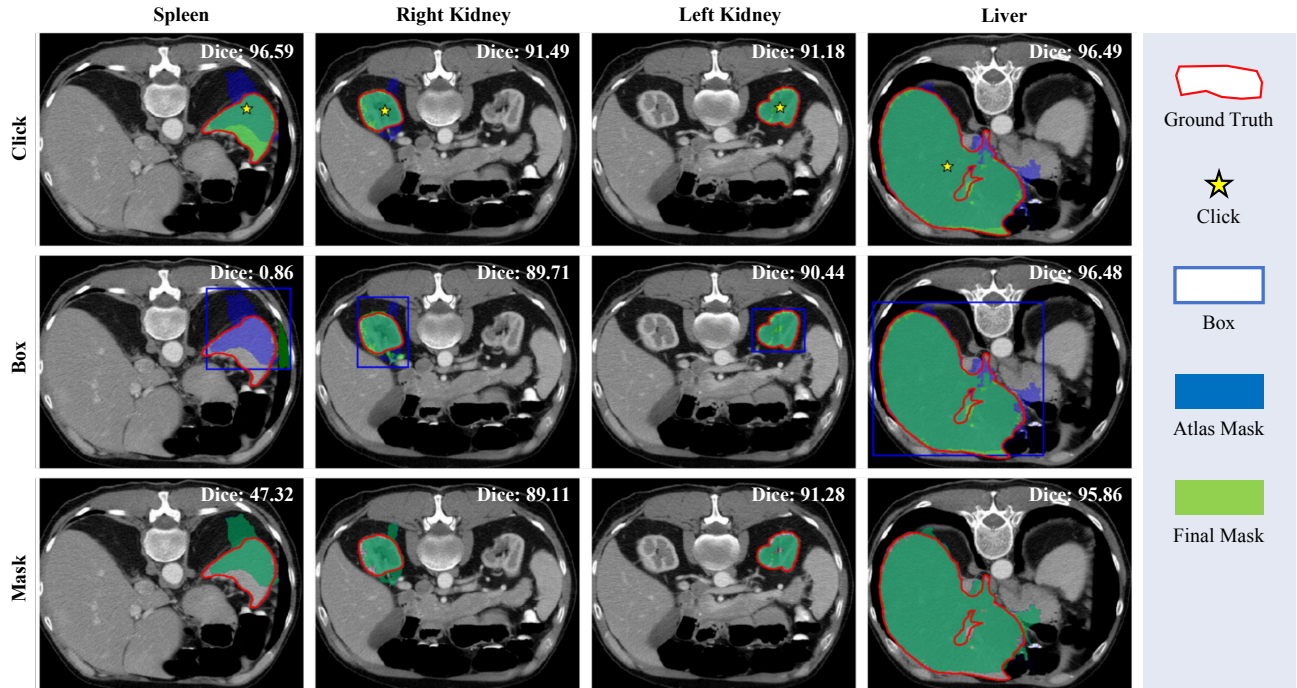


Figure 6. Qualitative results of AtlasSegFM with MedSAM2 using atlas-derived prompts on Abd-CT. Rows indicate prompt type (Click / Box / Mask); columns show Spleen, Right Kidney, Left Kidney, and Liver. Dice is reported per case. For MedSAM2, Click prompting is typically the most reliable initialization, while Box/Mask prompts can be less stable when the atlas prior is coarse.

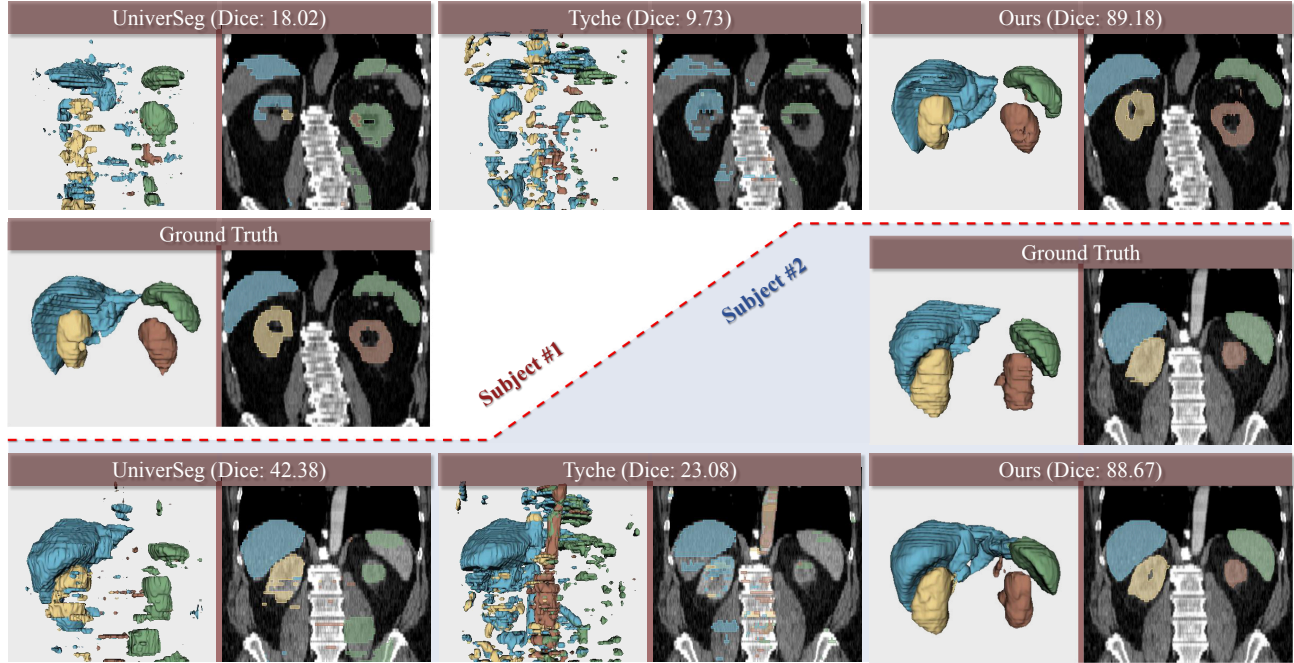


Figure 7. Visualization of our proposed 3D volumetric method vs. existing slice-wise 2D in-context baselines. 2D methods yield fragmented, cross-slice inconsistent masks, while AtlasSegFM produces coherent anatomy.

fails (0.86%), and the Mask prompt, despite containing dense spatial information, results in a suboptimal Dice score of 47.32%. A similar trend is observed in the Liver, where the Click prompt (96.49%) marginally outperforms the Mask prompt (95.86%). These results suggest that while the atlas effectively generates all prompt types, MedSAM2 is less robust to the dense noise potentially introduced by full mask priors and performs optimally when initialized with sparse point-based guidance provided by our method.

7. Additional Visualizations

Advancing beyond 2D ICL methods. Current in-context learning methods for medical image segmentation, such as UniverSeg [3] and Tyche [29], perform well on 2D datasets. However, their 2D architectures struggle to effectively capture the full spatial context required for accurate segmentation in 3D medical data. In contrast, our AtlasSegFM is designed to operate directly on 3D volumes, giving it a natural advantage in modeling global anatomical structures. We adopt the official code and pretrained weights of UniverSeg and Tyche, which operate using 2D context slices. To ensure a fair comparison, we provide each with a set of 2D slices that collectively cover all slices of the 3D atlas support. Following the standard protocol for extending 2D methods to 3D volumes [29], inference on the query volume is performed slice-by-slice.

As shown in Fig. 7, our AtlasSegFM significantly outper-

forms UniverSeg and Tyche, achieving higher Dice scores and more accurate and spatially consistent segmentation results. Quantitatively, our method achieves much higher Dice scores (*e.g.*, 89.18% vs. 18.02% and 9.73% in the first case), demonstrating superior segmentation accuracy. Spatially, the 2D methods produce fragmented and inconsistent results across slices whereas our method generates coherent and anatomically accurate masks. Visually, the reconstructed 3D shapes from UniverSeg and Tyche exhibit severe artifacts and distortions, while our method produces smooth and realistic structures closely matching the ground truth.

Failure case analysis. Despite its strengths, our method occasionally encounters challenges in certain difficult cases. As shown in Fig. 8, the first row presents two examples from the Abd-CT dataset [16] where our method generates incorrect or incomplete segmentations. Our method misclassifies the right kidney as part of the liver in the first example and fails to segment the spleen or left kidney in the second example. These errors are likely caused by substantial discrepancies between the query volume and the atlas, including anatomical variations, intensity distributions, or shape deformations. When the anatomy of the query volume deviates substantially from that of the atlas, such as in cases of patient-specific variations or deformations, the model struggles to generalize and accurately distinguish adjacent organs with similar intensities or poorly defined boundaries.

The second row of Fig. 8 presents examples from the AVT dataset [28], where our method fails to segment critical

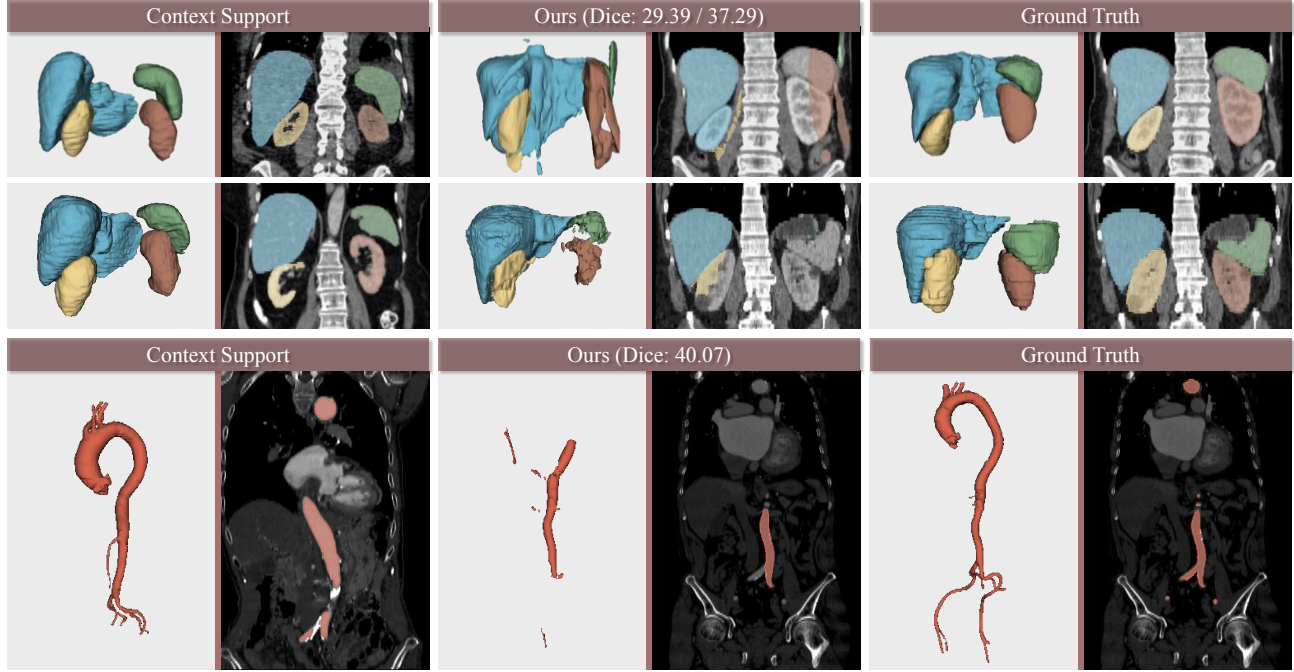


Figure 8. Representative failure cases. Top: Abd-CT—large atlas–query discrepancies can cause adjacent-organ confusion or missing organs. Bottom: AVT—complex vascular geometry (thin branches/sharp curvature) can lead to incomplete aortic-arch segmentation.

portions of the aortic arch, leading to incomplete reconstructions. This limitation can be attributed to the complexity of vascular structures, characterized by elongated geometries, fine branches, and sharp curves, which pose significant challenges for accurate segmentation.

These failure cases indicate that our method still has room for improvement, particularly in handling significant atlas–query differences and complex anatomical structures. To address these issues, future work could explore multi-atlas fusion techniques to better represent diverse anatomical variations and reduce dependency on any single atlas. Additionally, improved atlas–query registration methods could enhance spatial alignment, minimizing errors caused by anatomical mismatches. Incorporating prior shape knowledge or constraints for specific structures, particularly for vascular and organ geometries, could further improve segmentation accuracy and robustness in challenging scenarios.

8. Analysis of Registration Modules

The quality of the context prompt depends heavily on the registration step. In our method, we employ a deep-learning-based test-time optimization strategy derived from VoxelMorph [1]. Here, we justify this choice by comparing it against a traditional, industry-standard registration method: Symmetric Normalization (SyN) implemented via PyANTs (Advanced Normalization Tools). We replaced our VM-based module with PyANTs SyN+A/SyN+RA/SyN-

Only registration while keeping the rest of the AtlasSegFM pipeline (Prompting + FM + Fusion) identical.

As presented in Table 7, we observe that our proposed deep-learning-based optimization strategy significantly outperforms traditional registration approaches in terms of segmentation accuracy. Specifically, the SyN-Only setting, which lacks rigid or affine initialization, fails to establish a reasonable correspondence, resulting in a poor Atlas-Only Dice of 17.28%. This highlights the necessity of global alignment prior to deformable registration in traditional pipelines. While including affine transformations (SyN+A and SyN+RA) improves the Atlas-Only Dice to approximately 41%, it still lags behind our method (58.58%) by a large margin.

Furthermore, our method demonstrates superior stability. In our experiments on the Abd-CT dataset, we observed that both SyN+A and SyN+RA failed to converge or produced severely distorted deformation fields in 3 specific cases, leading to registration failure. In contrast, our test-time optimization strategy successfully registered all images, exhibiting higher resilience to anatomical variations.

To provide a more intuitive understanding of these performance gaps, we present a qualitative comparison in Fig. 9. The visualization clearly demonstrates the limitations of traditional registration in this context. For instance, the SyN-Only method (last column) fails catastrophically in multiple cases, yielding near-zero Dice scores, indicating a complete inability to locate the organ without prior rigid alignment.

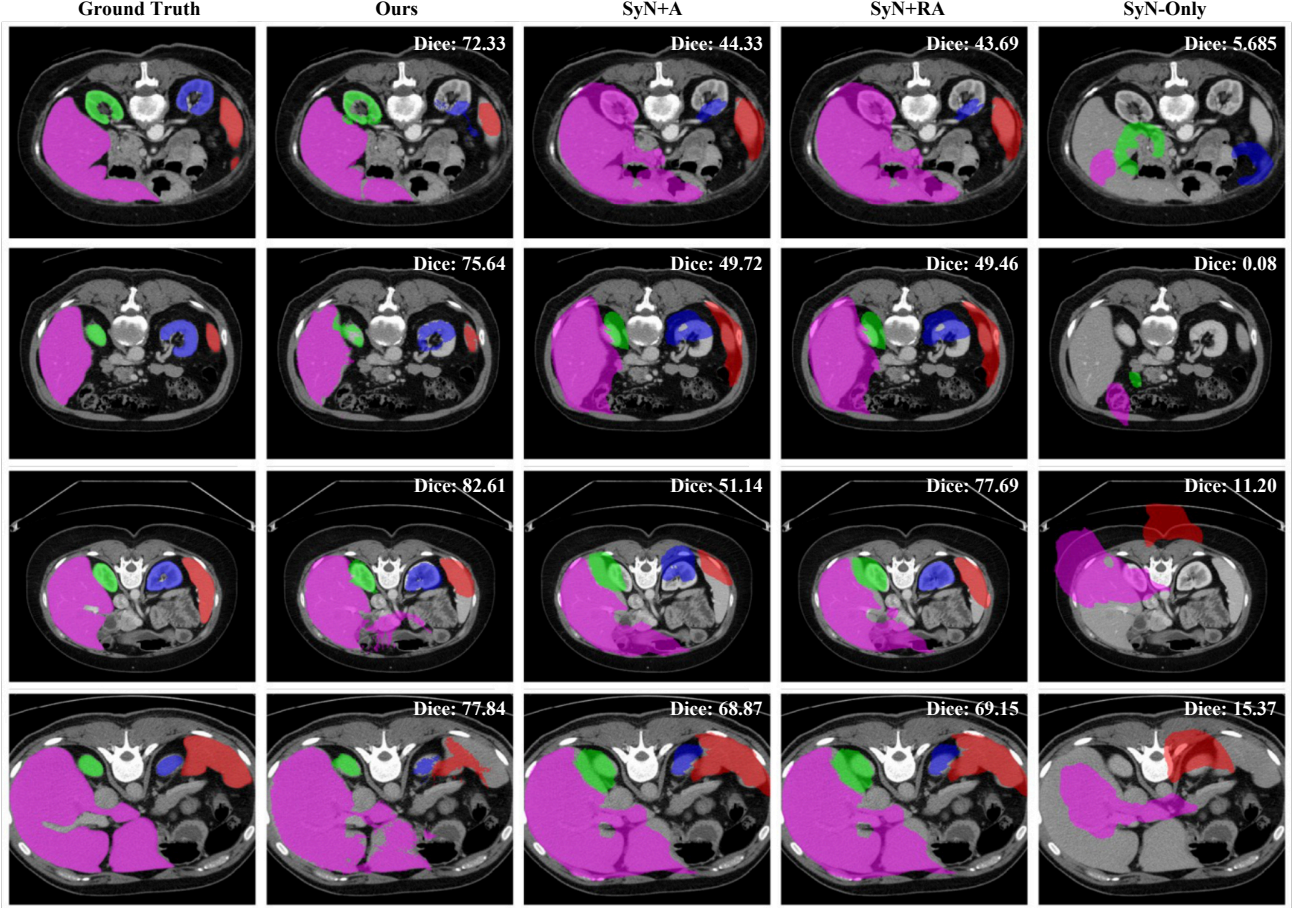


Figure 9. Visual comparison of different registration strategies. We compare the atlas masks generated by our proposed test-time optimization method against standard ANTs-based methods (SyN+A, SyN+RA, and SyN-Only). The Dice score for each specific case is annotated above the mask. Our method consistently produces accurate structural priors (Dice $> 70\%$), whereas traditional methods often struggle with boundary alignment (SyN+A/SyN+RA) or fail to localize the organ entirely (SyN-Only).

Table 7. Registration backend comparison on Abd-CT dataset. We report the quality of the atlas prior (Atlas-Only Dice) and the end-to-end impact after prompting + FM + fusion (Final Fusion Dice). Symmetric normalization with different settings: SyN+A (Affine + deformable transformation), SyN+RA (Rigid + Affine + deformable transformation), SyN-Only (no rigid or affine stages).

Registration Method	Atlas-Only Dice (%)	Final Fusion Dice (%)	Registration Time (min/image)
SyN+A	41.65	52.87	1.04
SyN+RA	41.13	51.82	1.13
SyN-Only	17.28	24.74	0.98
Ours	58.58	72.91	1.41

Even with affine initialization, SyN+A and SyN+RA often struggle to match the precise boundaries of the target organs, frequently resulting in Dice scores hovering around 40–50%. In contrast, our method (second column) consistently produces well-aligned masks that closely resemble the Ground Truth, achieving Dice scores above 72% across the presented examples. These accurate warped results provide high-quality prompts for the subsequent Foundation Model, ensuring more reliable segmentation guidance.

The registration quality directly impacts the final segmentation of the Foundation Models. The superior prompts provided by our registration module enables the AtlasSegFM framework to achieve a Final Fusion Dice of 72.91%, whereas the best-performing traditional baseline (SyN+A) only reaches 52.87%. Although our method incurs a slight increase in inference time (1.41 min/image vs. 1.04 min/image for SyN+A), this marginal cost is justified by the substantial +20% improvement in final segmentation accuracy.